

Automated Decision Support System for Lung Cancer Detection and Classification via Enhanced RFCN With Multilayer Fusion RPN

Anum Masood, Bin Sheng , Po Yang, Ping Li , *Member, IEEE*, Huating Li , Jinman Kim , and David Dagan Feng , *Fellow, IEEE*

Abstract—Detection of lung cancer at early stages is critical, in most of the cases radiologists read computed tomography (CT) images to prescribe follow-up treatment. The conventional method for detecting nodule presence in CT images is tedious. In this article, we propose an enhanced multidimensional region-based fully convolutional network (mRFCN) based automated decision support system for lung nodule detection and classification. The mRFCN is used as an image classifier backbone for feature extraction along with the novel multilayer fusion region proposal network (mLRPN) with position-sensitive score maps being explored. We applied a median intensity projection to leverage three-dimensional information from CT scans and introduced deconvolutional layer to adopt proposed mLRPN in our architecture to automatically select the potential region of interest. Our system has been trained and evaluated using LIDC dataset, and the experimental results showed promising detection performance in comparison to the state-of-the-art nodule detection/classification methods, achieving a sensitivity of 98.1% and classification accuracy of 97.91%.

Index Terms—Computer-aided systems, convolutional neural network (CNN), lung cancer, nodule classification.

I. INTRODUCTION

LUNG cancer is considered to be a major cause of death worldwide. Almost 1.6 million people die in a year due to pulmonary cancer. In 2018, pulmonary cancer has caused 142 670 deaths alone in the USA [1]. Pulmonary cancer is a disease indicated by the uncontrollable growth of abnormal pulmonary cells. A most effective method for lung nodule detection in early stages is computed tomography (CT) scan owing to its ability to generate high-resolution three-dimensional (3-D) chest images. Detection of lung cancer in the initial stages is crucial to patient's survival but it is a tedious and difficult task since the radiologists manually mark nodule position and possibly miss lung nodules that have overlapping anatomical structures.

In the past decade, the lung cancer death rate is comparatively reduced owing to the advancements in the industrial applications used for lung cancer detection and diagnosis. Different commercially available computer-aided systems have the potential to tremendously increase the detection as well as the diagnosis accuracy even with high-dimensional lung cancer dataset without annotation features for classification. CAD system for nodule detection comprises computer-aided detection (CADE) and computer-aided diagnosis (CADx). The CADE aims to distinguish between the nodule candidates as nonodule (anatomical structures like tissues, blood vessels), whereas CADx characterizes these detected lesions and classifies them as benign or malignant tumors. The aim of these CAD systems primarily is to overall enhance the accuracy of cancer diagnosis by the radiologists while reducing the CT images interpretation time duration. In this way, these tools have become crucial to assist in their decision making.

With the introduction of deep learning techniques [2] particularly in object detection and feature extraction from big data, various computer-aided (CAD) systems based on deep learning are developed for real-world clinical use. These methods have significantly enhanced the quality and the efficiency of the healthcare sector particularly the screening process for lung cancer early detection. Although the innovations in pulmonary cancer are slow and unsteady in terms of survival rate as compared to the other cancer types, yet deep learning methods

Manuscript received September 30, 2019; revised January 15, 2020; accepted February 1, 2020. Date of publication February 21, 2020; date of current version September 18, 2020. This work was supported in part by the National Natural Science Foundation of China under Grant 61872241 and Grant 61572316, in part by the National Key Research and Development Program of China under Grant 2017YFE0104000 and Grant 2016YFC1300302, and in part by the Science and Technology Commission of Shanghai Municipality under Grant 18410750700, Grant 17411952600, and Grant 16DZ0501100. Paper no. TII-19-4473. (*Corresponding authors: Bin Sheng; Huating Li.*)

Anum Masood is with the Department of Computer Science and Engineering, Shanghai Jiao Tong University, Shanghai 200240, China, and also with the Department of Computer Science, COMSATS University Islamabad, Islamabad 45550, Pakistan (e-mail: anummasood@sjtu.edu.cn).

Bin Sheng is with the Department of Computer Science and Engineering, Shanghai Jiao Tong University, Shanghai 200240, China (e-mail: shengbin@sjtu.edu.cn).

Po Yang is with the Department of Computer Science, University of Sheffield, S1 4DP Sheffield, U.K. (e-mail: po.yang@sheffield.ac.uk).

Ping Li is with the Department of Computing, The Hong Kong Polytechnic University, Hong Kong (e-mail: p.li@polyu.edu.hk).

Huating Li is with the Shanghai Jiao Tong University Affiliated Sixth People's Hospital, Shanghai 200233, China (e-mail: huating99@sjtu.edu.cn).

Jinman Kim and David Dagan Feng are with the Biomedical and Multimedia Information Technology Research Group, School of Information Technologies, The University of Sydney, Sydney, NSW 2006, Australia (e-mail: jinman.kim@sydney.edu.au; dagan.feng@sydney.edu.au).

Color versions of one or more of the figures in this article are available online at <https://ieeexplore.ieee.org>.

Digital Object Identifier 10.1109/TII.2020.2972918

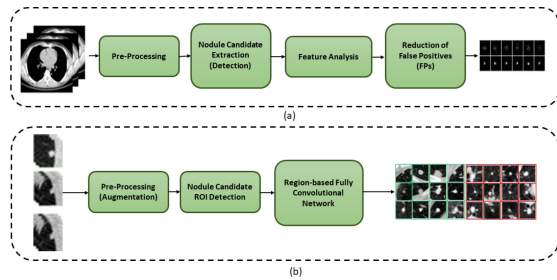


Fig. 1. (a) Basic stages of CAde system for lung nodules. (b) Stages of our proposed CAde system.

have promising results and the detection systems based on deep learning techniques have declined the lung cancer death rate by the factor of 22% in the last five years. In this article, we have proposed a novel CAD system for pulmonary nodule detection and classification. The key contributions of this article are listed as follows.

- 1) A novel deep convolutional neural network (CNN) based model is proposed for early detection of lung cancer, which is capable of using 3-D spatial as well as contextual information yielding a larger amount of discriminating feature map for nodule candidates detection.
- 2) Novel multilayer fusion region proposal network (mLRPN) is proposed for the selection of potential region of interest (RoI) with position-sensitive score maps (PSSM) to achieve high accuracy in nodule classification. We applied novel median intensity projection (MIP) to leverage 3-D information from CT images, and integrated deconvolutional layer to adopt mLRPN for automatic RoI selection.
- 3) The performance of the proposed CAD system is validated in two modes: multidimensional region-based fully convolutional network (mRFCN) stand-alone and mRFCN cloud-based. Testing of both modes is done on LIDC dataset and clinical dataset from Shanghai Sixth People's Hospital (SPH). Furthermore, experimental results for the performance of the proposed method on the LIDC dataset show high precision and reduced false positive (FP) rate to a significant extent in comparison to the state-of-the-art nodule detection and classification methods.

II. RELATED WORK

In general, any CAde system for lung cancer comprises four phases: preprocessing, lung segmentation, analysis of feature set, and candidate nodule detection; on the other hand, CAD systems have two stages: nodule candidate detection and FP reduction (see Fig. 1). For nodule detection, traditionally lung segmentation is done using 2-D geometrical level set active contour, morphological features, 2-D parametric deformable model, voxel clustering and multi-gray-level thresholding. The limitation of these models was their dependence on the image and inability to detect nodules overlapping anatomic structures [3]. Several researchers have proposed various CAde systems to

detect the lung nodules. Armato, III, *et al.* [4] proposed a CAde system that uses linear discriminant analysis (LDA) method on 187 nodules (juxtaleural and solitary nodules) resulting in a sensitivity of approximately 70% while having 9.6 FP per case. Suzuki *et al.* [5] used the dataset of 121 nodules (juxtaleural, juxtavascular, solitary, and ground-glass shaped lesions), whereas Kumar *et al.* [6] developed massive training artificial neural network (MTANN) for nodule detection. The initial nodule candidates are processed using filtering method in order to remove the FP results. Supervised approaches are also developed to reduce the FP but these methods have a high computational cost. Hierarchical VQ, LDA, ANN, and SVM are few supervised reduction methods that are used for FP reduction [7]–[10]. In recent years, deep learning is introduced in medical imaging; according to Setio *et al.* [11], there are numerous CAD systems using deep learning for nodule detection. CNN [12], fully convolutional networks (FCNs) [13], multicrop-CNN (MC-CNN) [14], and DFCNet [15] are CAD systems based on deep neural networks that are capable of classifying the detected nodules as benign or malignant tumors.

III. METHODS

A. Datasets

In the real application of CAD system, the screening stage is very crucial. Since it is a huge computation cost for using 3-D CT scans volume, an alternation of using source pictures in axis direction is applicable. Therefore, we combined three neighboring CT scans for each axis direction, respectively. The potential candidates, choice of search space can be further analyzed by selecting training sets of original CT scans.

B. Augmentation

In situations, where a limited amount of labeled data is available, neural networks tend to overfit training dataset, because these models have large quantities of parameters. An efficient way to tackle this problem is data augmentation. Although part of the resultant samples from data augmentation might be similar to each other. During the data augmentation phase, each RoI goes through a series of image transformations for label preserving, producing a huge amount of correlated newly acquired training data samples. Affine transformation namely translation, scaling and rotation are used. Mostly the training data samples obtained from data augmentation have a correlation; thus, this step is recommended for data overfitting reduction. We opted to augment malignant samples by cropping, duplicating, flipping, scaling and rotating copies in the training dataset. Specifically, among input batch, random rotation was performed for upsampling and downsampling. We resampled training and testing cases to 3 mm since having a common thickness method helped in attaining the homogeneity among all cases (training and testing), which further improved the dataset processing.

C. Architecture

1) *Multiview Combination*: Unlike traditional image classification problem where input channels are the same as the color channels of the image, CT scan generates gray-scale images. Another notion is that CT scans sets are originally 3-D in which z-axis discriminates different positions of lung nodule, whereas the input image sets are 2-D patches. Inspired by Hessian, we explore MIP [16] to combine information from three dimensions of CT scans. We defined θ as an image projected by MIP. With input image patch I , θ for three dimensions can be presented as

$$\begin{aligned}\theta(q, r) &= \text{med}_p I(p, q, r) \\ \theta(p, r) &= \text{med}_q I(p, q, r) \\ \theta(p, q) &= \text{med}_r I(p, q, r)\end{aligned}\quad (1)$$

where med denotes median operator. Different views can provide different information, whereas patches in combination with different dimensions can provide the space distribution of tumor tissues. In order to construct input image sets with three channels, we connected three MIP projected images together: $\theta = [\theta(q, r), \theta(p, r), \theta(p, q)]$.

The proposed mLRPN is designed to improve the original RPN from faster R-CNN [17] is designed to overcome the limitation of the previous related work targeted for object detection, i.e., faster R-CNN. Although the proposed work is inspired from the ResNet of faster R-CNN yet it has replaced 2-D with 3-D convolution layers. CT images can be processed by proposed MIP method to interactively viewing volumes of CT data, in which the CT number of each pixel is given by the minimum number of CT through the volume. Furthermore, unlike the faster R-CNN, the proposed mRFCN uses mLRPN, which improves the ROI selection thus improving the performance of detection by the proposed method. Additional deconvolutional layer improved the original RPN from faster R-CNN. The deconvolutional layer upsampled the features learned from the input. Traditionally, faster R-CNN depends on the skip connection linked with the deconvolution layer on the upsampling for generating initial results but the deconvolution layer is unable to recover the small-sized objects such as nodules that are lost after the downsampling. Therefore, they cannot accurately detect small-sized nodules. In our proposed method, we used deconvolutional layer that ensured the recovery of any loss of small objects such as lung nodules in the downsampling process. The challenge for faster R-CNN in case of lung nodule detection is that it cannot detect the diverse sized objects using limited labeled dataset. To mitigate this we proposed a novel method, mLRPN has improved feature extraction (multiresolution) and we used multiple layers for region proposal generation, i.e., multiangle, multisize and multishape. For the efficient selection of the ROI, we proposed to merge all the RoIs that were extracted from multilayers in a single layer, as shown in the overview of the mRFCN in Fig. 2.

2) *Multilayer Region Proposal Network*: A prevalent method for selecting RoI is to split original CT scans into small sample windows: 8×8 , 16×16 , and 32×32 . For our proposed work, we selected the mini-window, whose spatial window contains

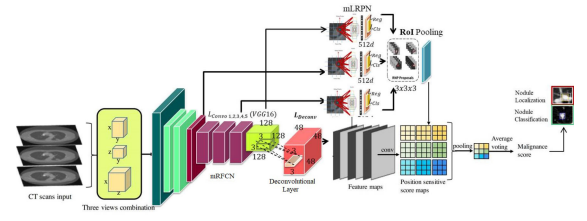


Fig. 2. Overview of the mRFCN architecture.

the central of malignant nodule according to the marked-up annotation from experienced thoracic radiologists, as positive training or testing samples. Such a strategy has an obvious disadvantage that if a specific nodule is larger than prefixed sample window or some nodule is located across two sample windows, then it will be discarded. This disadvantage will lead to inaccurate construction of training or testing sets, and further lead to low classification performance. In order to address the problems mentioned above and select several RoI efficiently, we proposed a novel mLRPN. In the mLRPN, in order to improve the ability to detect nodules of different scales, shape, and orientation, we designed a three-layer multi-RPN: multi-size v_{L1}^u , multiangle θ_{L1}^g , and multishape d_{L3}^j , which generate rectangular object proposals set using the image (irrespective of size) as its input, and further calculates objectness value for each set [17]. We observed that malignant nodule occupy a relatively small proportion of CT scans compared to conventional object recognition tasks where object takes up a larger space in the image. Since VGG-16 Net contains several max pooling layers, it inevitably reduce the image size [18], resulting in the relatively small nodule distorted. Gaining inspirations from the previous success of Long *et al.* [19], we proposed a deconvolutional layer, four kernel size, and four stride size, to be added after the last feature extracting layer. This deconvolutional layer is aimed to recover the original CT scans size by upsampling (see Fig. 2 for our proposed system).

According to [20], we use a tiny network N to slide through the activation (feature) map output M_{out} by the final added deconvolutional layer. We also defined this tiny network N to take 3×3 spatial windows of the input activation(feature) map M_{in} with each spatial window w being mapped to 512-D feature. The feature will be fed into box-classification layer and regression layer (reg), respectively. As for the choice for anchor [21] size shown in Fig. 3, we explore large quantities of nodule boundary size, and generate six different sizes v_{L1}^u (u represents anchor size) of reference boxes centered at each sliding window location for our multisize layer. In order to contain nodules of different malignant level, we choose anchor sizes of 4×4 , 8×8 , 12×12 , 20×20 , 26×26 , 32×32 , respectively (see Fig. 3). As the nodule spreads in all direction therefore, we proposed a multiangle layer, in which we rotated RPN with 12 different angles θ_{L2}^g , where g represents angle, i.e., 0° , 30° , 60° , 90° , 120° , 150° , 180° , -150° , -120° , -90° , -60° , and -30° rotation from the center of sliding window. Lastly, we proposed multishape layer d_{L3}^j where j shows different shapes based on the anchor's width to height ratio: 1:1, 2:1, and 1:2.

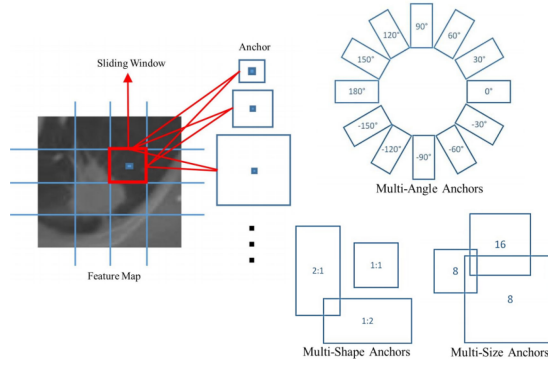


Fig. 3. Our proposed anchor in mLRPN.

3) Multidimensional Region-Based Fully Convolutional Network: With mLRPN proposing RoI, we apply RFCN [22] to predict the presence of nodule or the malignancy level if nodule exists. Our architecture is inspired from ResNet-101 [23], which is based on the VGGNet, comprising 3×3 filters with the convolutional network. In ResNet-101, if the filters and layers are comparable then the feature map size remains the same but in order to maintain time complexity for each layer when activation map size is halved, the number of the filters should be doubled. In mRFCN, we excluded the fully convolutional layer and the mean pooling layer for efficient computation of the feature maps. In case of similar dimensions for both the output and input, the identity alternatives can be directly used

$$q = \mathbb{F}(p, \{W_i\}) + p \quad (2)$$

where p and q denote input and output vectors, respectively, that are fed into and considered by each network layer. The function $\mathbb{F}(p, \{W_i\})$ shows the residual mapping that is to be learnt. There are two alternate solutions in case the input dimensions increase. If no extra parameters are already present then the identify mapping's dimensions are increased by zero entries padding. Another way is to add 1×1 convolutional layer to match the dimension with shortcut projection. The stride for both options is 2. Unlike ResNet-101, our proposed model uses convolutional layer solely to compute the feature map, therefore, the learnable weights are computed using convolutional layers and shared on the whole image. The architecture design of mRFCN is shown in Fig. 4.

Using the radiologist annotations, we add a $k \times k(5 + 1)$ -channel convolutional layer (4×4) as the output layer to generate PSSM, where 4 represents five malignant level of lung nodule, 1 represents nonnodule, and we divide mLRPN proposed RoI into 4×4 grid cell. Specifically, for 32×32 proposed rectangular, each divided grid has the size of 8×8 . Therefore, $4 \times 4 \times 6$ score maps were generated, and we used the average pooling operation to calculate the relevance score to six categories for each split bin

$$\zeta_c(w, h | \phi) = \sum_{(a,b) \in \text{bin}(w,h)} z_{w,h,c}(a + a_0, b + b_0 | \phi) / n \quad (3)$$

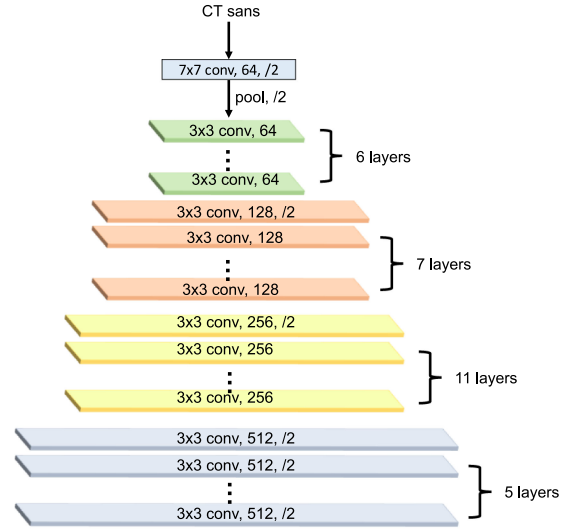


Fig. 4. Detailed configuration of our proposed mRFCN.

where ϕ denotes parameters of the network, $\zeta_c(w, h | \phi)$ is the relevance score of (w, h) th bin to malignant category c , $z_{w,h,c}$ is the score map generated by last convolutional layer, (a_0, b_0) is the top-left corner of RoI, and n denotes the total pixel number in the bin. With $4 \times 4 \times 6$ relevance scores ζ being calculated, we decide the malignancy level of the RoI by average voting and also apply cross-entropy evaluation for ranking of RoI

$$\zeta_c(\phi) = \sum_{w,h} \zeta_c(w, h | \phi) \quad (4)$$

$$\xi_c(\phi) = \exp(\zeta_c(\phi)) / \sum_{\iota=0}^5 \exp(\zeta_{\iota}(\phi)) \quad (5)$$

where $\zeta_c(\phi)$ denotes the relevance score for RoI to class c , and $\xi_c(\phi)$ is the softmax response for class c .

Following [21] and [23], we also applied bounding box regression to generate 4-D bounding box vector $t = (t_x, t_y, t_w, t_h)$; the parameters are defined as

$$\begin{aligned} t_x &= (x - x_a) / w_a \\ t_y &= (y - y_a) / h_a \\ t_w &= \log(w / w_a) \\ t_h &= \log(h / h_a) \end{aligned} \quad (6)$$

where (x, y) denotes the box's central position, and w represents the width and h shows the box height. The variables above with subscript a are the corresponding parameters for anchor box (see Fig. 3). We add a sliding $4 \times 4 \times 4$ -D convolutional layer for bounding box regression. After we obtained $4 \times 4 \times 6$ score maps bank, we simply use position-sensitive RoI pooling on them, further we get $4 \times 4 \times 4$ -D vector for each RoI. The position-sensitive RoI pooling layer is used to leverage position-sensitive score in each grid. The whole computation process is almost cost-free since there is no supervised learning layer following the RoI layer.

Algorithm 1: Multidimensional Region-Based Fully Convolutional Network Training Procedure.

```

1: procedure MULTIDIMENSIONAL REGION-BASED
  FULLY CONVOLUTIONAL NETWORK TRAINING
  PROCEDURE( $B, b, n, S, \alpha, \beta_1, \beta_2$ )
2:   Inputs:
3:    $B$ : RoI sample batch size;
4:    $b$ : mini-batch size;
5:    $S$ : Rescale image size;
6:    $\alpha$ : Adam stepsize;
7:    $n$ : Training iteration;
8:    $\beta_1, \beta_2 \in [0, 1)$ : Exponential decay rate for moment
  estimates;
9:   Initialization:
10:  Initialize  $\tilde{w}^0 = 0$  (Initialize network parameter
  vector);
11:  Pre-process dataset:
12:  Construct 3-dim dataset using Median Intensity
  Projection according to Eq. (1);
13:  Rescale dataset into  $S$ ;
14:  for  $s = 0, 1, 2, \dots, n$  do
15:    Forward Pass:
16:    Generate feature map with
  multidimensional-RFCN architecture;
17:    Generate  $M$  Region of Interest;
18:    for  $m = 0, 1, 2, \dots, M$  do
19:      Construct loss function for  $\text{RoI}_m$  using Eq. (6);
20:    end for
21:    Backpropagation:
22:    RoIs sorting by loss (positive RoIs and negative
  RoIs);
23:    Selection of highest loss  $\mathbb{L}$  in set  $B$  RoIs;
24:    Gradient estimation  $g_s = \frac{\sum_{i \in B} \nabla \mathbb{L}_i}{B}$ ;
25:     $m_{s+1} = \beta_1 \cdot m_s + (1 - \beta_1) \cdot g_s$  (Updating of
  biased  $1^{st}$  moment estimate)  $\triangleright$  Adam process;
26:     $v_{s+1} = \beta_2 \cdot v_s + (1 - \beta_2) \cdot g_s^2$  (Updating of biased
   $2^{nd}$  raw moment estimate);
27:     $\hat{m}_{s+1} = m_{s+1} / (1 - \beta_1^{s+1})$  (Computation of
  bias-corrected  $1^{st}$  moment estimate);
28:     $\hat{v}_{s+1} = v_{s+1} / (1 - \beta_2^{s+1})$  (Compute bias-corrected
   $2^{nd}$  raw moment estimate);
29:     $\tilde{w}^{s+1} = \tilde{w}^s - \alpha \cdot \hat{m}_{s+1} / (\sqrt{\hat{v}_{s+1}} + \epsilon)$ ;
30:  end for
31:  return  $\tilde{w}^n$  (the tuned network parameter);
32: end procedure

```

D. Loss Function

In the training process, with RPN to provide region proposal, we define our loss function by merging box regression as well as the cross-entropy loss

$$\{L\}_{t,\xi} = -\log(\xi_{c^*}) + \left\{ \frac{1}{N_r} \right\} \sum \{L\}_r(t, t^*) \quad (7)$$

$$\{L\}_r(t, t^*) = \begin{cases} 0.5(t - t^*)^2, & \{\text{if } |t - t^*| < 1\} \\ |t - t^*| - 0.5, & \{\text{otherwise}\} \end{cases} \quad (8)$$

where the left part of (7) denotes classification cross-entropy loss [23], N_r is the input number of reg, \mathbb{L}_r is similar to the bounding box regression loss as presented in [17], and t^* denotes ground-truth values. Positive samples are represented by RoIs that have an intersection-over-union protrude with ground-truth box of minimum 0.5, and alternatively, negative. In our mRFCN training procedure, the computation cost of RoI is negligible, which enables the example mining to be cost free. We first construct the 3-D dataset using MIP and then re-scale the dataset as predefined size. We followed the standard procedure to iteratively tune our network parameters. In the forward pass, the input CT scans are generated with higher dimensional feature map and M RoIs are generated using RPN, we then follow the loss function to evaluate M proposals loss. After sorting RoIs (both the positives RoIs and negatives RoIs) by loss, the highest loss of B RoIs is selected. In order to leverage the gradient information from selected batches, we perform average gradient operation on the B samples and use it as the input gradient estimation for Adam process to iteratively optimize our designed neural network. The detailed training procedure is summarized in Algorithm 1.

E. Implementation Details

We initialized the network using LIDC pretrained basic model and the weights of layers in our proposed model. In the first step we freeze all layers in basic model with only training the layers of mRFCN and mLRPN. Second, the whole network is trained within two stages by decreasing learning rate. Following the common used settings in faster R-CNN, the input images are first normalized and then we employed mRFCN architecture. The experiment was conducted on Ubuntu 16.04.3 LTS with four processors, Intel(R) Xeon(R) CPU E5-2686 v4 @ 2.3 GHz, and 64 GB total memory space. Our model is trained on Tesla K80 with 12 GB memory. As for RFCN, we choose to use Intel Extended Caffe since the convolution layer, max pooling layer and fully connection layer in Caffe is self-adaptive to the shape of input. Some other common libraries used include numpy 1.13.1, SimpleITK 1.1.0, pandas 0.19.2, sklearn 0.18.2. The training process of mRFCNN is done in 3 hours on Nvidia Tesla K80 graphic card. Training process used standard backpropagation using stochastic gradient descent (weight decay: 0.00045, momentum: 0.12, and learning rate of 0.02 with the increasing factor of 15 after 500 iterations).

F. Cloud-Based Multidimensional Region-Based FCN

For clinical validation of mRFCN, we collaborated with SPH. As a stand-alone CAD system, our proposed method performed well but to further improve the performance of our proposed method, we integrated cloud computing (Infrastructure as a Service by providing virtual machines, and Software as a Service by giving our mRFCN model) into our CAD system as shown in Fig. 5. In cloud-based mRFCN, we have four modules: data submission, online medical reports submission by radiologists of SPH, CAD result access, and physicians feedback. First, the medical systems from SPH sent CT images of patients to the cloud storage using the router gateway. To record the physiological information of patients, we used BAN comprising multiple

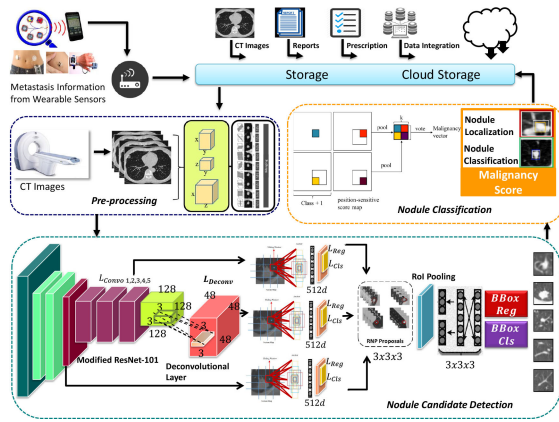


Fig. 5. Pipeline for our proposed decision support system. First, we used body area network (BAN) and CT scan to collect comprehensive physiological information and CT images of patient, which were forwarded to cloud storage. Second, we applied affine transformations on CT-images for data augmentation. Furthermore, we preprocessed CT images using multiview combination. We used mRFCN model on these preprocessed CT images for nodule candidate detection. Meanwhile, mLRPN with three layers of designed multianchors are applied to obtain the RoI proposals. Finally, we utilize PSSM to classify detected nodules into two classes, i.e., benign and malignant. The marked location of the nodule and the classification results are stored on the cloud for the physicist's reference for diagnosis and treatment.

sensors attached to patients body. Furthermore, gateways are used to forward this acquired physiological data to cloud storage for processing. Afterward, our proposed mRFCN model is used to screen the CT images for nodules. Cloud storage enabled the storage of a vast amount of clinical data on which the proposed method was trained, the CT-images are processed by the mRFCN resulting in the marked nodules and their classification as malignant or benign. These results are considered as second opinion by the radiologists for making final diagnosis decision. The diagnosis decision is sent for real-time analysis by the physicians who determine the disease level and send the regular check-up notifications, reports, as well as treatment prescription to the patient. The regular check-up reports, disease status, and the response of the patient to the treatment is stored on the cloud storage for further data analysis and improvement of our proposed CAD system. Currently, we are able to deploy ten VMs, and 24 processing units (cores) in our dedicated cloud back-end. For each case, the complete processing time is 11–12 min. An open-source tool, HTCondor, was used for real-time optimization and monitoring of computing resources, and thus the users have updated responsive CAD system.

IV. RESULTS AND DISCUSSIONS

Every year, around 1.59 million deaths are caused by Lung Nodule. It is essential to use CAD system to help radiologists to detect and diagnose pulmonary cancer. For developing a reliable CAD system, it should provide high performance in terms of diagnosis speed, quantity, accurate evaluation and overall low error rate. In state of the art, the prevalent criteria for CAD system performance are two kinds of rate: sensitivity and FP.

TABLE I
LUNG NODULE FEATURES FROM RADIOLOGIST

| Features | Descriptions |
|--------------------|-------------------------------|
| Internal structure | Soft tissue, fluid |
| Calcification | Popcorn, solid |
| Margin | Poorly defined, intermediate |
| Lobulation | Marked, intermediate |
| Spiculation | Marked, intermediate |
| Sphericity | Linear, ovoid |
| Texture | Non-solid, Part solid/(mixed) |

The performance of the proposed CAD system is validated in two modes: mRFCN stand-alone and mRFCN cloud-based. Testing of both modes is done on LIDC dataset and clinical dataset. Furthermore, the nodule detection results of the proposed CAD system are compared with the state-of-the-art CAD systems using free-response receiver operating characteristic (FROC) curve including average sensitivity and number of false positives per scan (FPs/scan) as evaluation metric, where detection is considered a true positive if the location lies within the radius of a nodule center, whereas the nodule classification performance analysis is done using area under the ROC curve (AUROC) that shows the performance of our proposed method on candidates' classification as nodules or nonnodules. In CAD system, when predicting the existence of nodule, we make comparison with the ground-truth annotation, the FP ratio is the probability of falsely rejecting the null hypothesis for a particular test.

We calculate FP with the ratio between the number of non-nodule samples are mistakenly predict as lung nodule with certain level of malignancy and the total amount of non-nodule samples. We define FP rate as

$$\frac{FP}{N} = \frac{FP}{FP + TN} \quad (9)$$

$$SP = \frac{TP}{TP + FN} \quad (10)$$

where SP, FP, FN, and TP denote sensitivity, false positive, false negative, and true positive rate, respectively. In our experiment, if a sample with nodule is not predicted as disease in our CAD system, it is FN. If a sample with nodule is predicted correctly, it represents TP. The performance evaluation of our proposed CAD system is done on the subset of LIDC-IDRI [24]. We consider the 1000 CT subsets, from LIDC-IDRI-0001 to LIDC-IDRI-1000. Note originally LIDC-IDRI contains 1018 CT scans sets in total. Every CT scan has around 300 slices, and each slice of which is gray-level picture in size of 512*512, the slice thickness is 3 mm. We reconstruct all the images using sharp kernel (Siemens B50 kernel). For testing the performance accuracy of our CAD system for detecting pulmonary nodules, we excluded the CT scans that are inconsistent in slice spacing or have missing slice. After that procedure, we finally make a list of 892 CT scans. We significantly reduced the quantity of the non-nodule data samples since they are the majority component of CT scans, which impact the accuracy of CAD system with large quantity of presence. We define distinct features in appearance of nodule in Table I.

TABLE II

CLASSIFIERS' ACCURACY, SENSITIVITY, AND FPs/SCAN COMPARISON TO DETECT LUNG CANCER BASED ON LEAVE-ONE-OUT VALIDATION METHOD

| Classifiers | Accuracy (%) | Sensitivity (%) | Fps/Scan |
|------------------------|--------------|-----------------|----------|
| CNN [12] | 80.8 | 79.6 | 3.63 |
| MTANNs [6] | 88.6 | 86.53 | 2.62 |
| FCN [13] | 91.2 | 91.14 | 3.16 |
| MC-CNN [14] | 87.14 | 77.3 | 2.97 |
| mRFCN | 92.1 | 94.4 | 2.21 |
| mRFCN (Using mLRPN) | 97.91 | 98.1 | 2.19 |

TABLE III

PERFORMANCE COMPARISON OF THE PROPOSED CADE WITH THE STATE-OF-THE-ART CAD SYSTEMS TO DETECT LUNG CANCER BASED ON LEAVE-ONE-OUT VALIDATION METHOD

| CAD systems | Sensitivity (%) | Fps/Scan |
|---------------------|-----------------|----------|
| Suzuki et al. [5] | 80.3 | 4.8 |
| Ye et al. [7] | 90.2 | 8.2 |
| Messay et al. [8] | 80.4 | 3.0 |
| Cascio et al. [9] | 87 | 6.1 |
| Han et al. [10] | 82.7 | 4.0 |
| mRFCN | 94.4 | 2.21 |
| mRFCN with mLRPN | 98.1 | 2.19 |

We use the leave-one-out validation method to validate our CAD classifier's generalization performance. We randomly divided the CT scans from our dataset into training sets and testing sets, training sets are used to train our CAD classifiers and testing sets are used to validate the performance of CAD classifiers. The effectiveness of mRFCN is verified by comparing with existing methods CNN [12], MTANNs [6], FCN [13], and MC-CNN [14]; the results are depicted in Table II. From Table II, we can deduce that mRFCN's performance is highest achieving a sensitivity of 92.1% and 94.4% accuracy with a lowest FP rate of 2.21 per CT scan among the state-of-the-art CAD system. The results indicate the superiority of mRFCN as CAD system for nodule detection. The comparison between "mRFCN" and "mRFCN (using mLRPN)" indicates that the proposed CAD system with three-layer multianchor (multisize, multiangle, multishape) parameter setting performs better for RPN in candidate selection both in terms of sensitivity and accuracy, which are recorded to be 98.1% and 97.91%, respectively.

Although different CAD systems are experimented on variable datasets that make the relative comparison a difficult task, we still made the comparison between our proposed system with previously published CAD systems to investigate the perspectives of our mRFCN system since the average FPs/scan is comparable and the comparison results are shown in Table III. In the experiment with nodule detection, data analysis is different from the binary classification problem that each image might contain multiple lung nodule and more than one FPs/scan. Therefore, the conventional ROC curve is not suitable to analyze the performance of our CAD system. In order to handle this problem, we apply FROC analysis [25]. A prevalent method [11] for

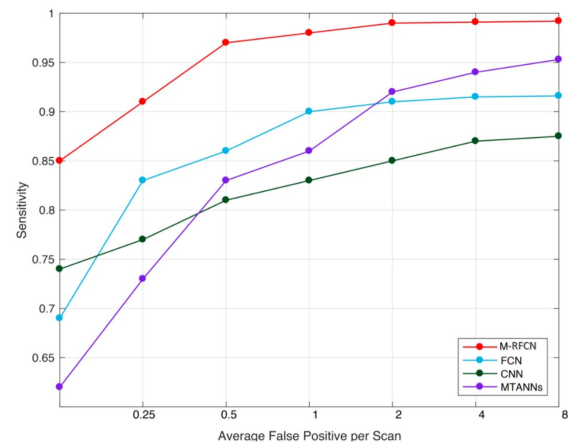


Fig. 6. FROC curve comparison between our proposed mRFCN system and other existing CAD system.

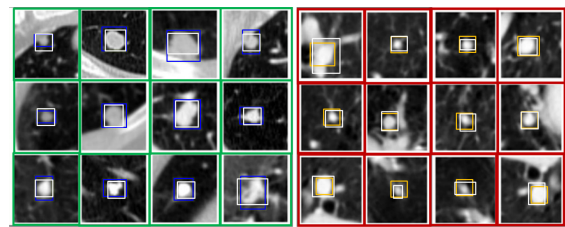


Fig. 7. Nodules detected as true positives malignant (green outline) and true positives benign (red outline) from the proposed CADE system. White boxes mark the ground truth and results produced by our CADE systems are marked by blue or yellow boxes. Blues and yellow boxes are, respectively, denoting the malignant and benign nodules on the basis of malignancy score at 98.1% sensitivity.

evaluating mRFCN curve is used. The sensitivity of the FROC curve is a function plotted on the mean number of FPs/scan. The mean FROC-score is calculated as the sensitivity mean at seven FPs: 8, 4, 2, 1, 1/2, 1/4, and 1/8 FPs/scan. Tables IV and V list the quantitative results of our proposed approach in comparison with others.

Fig. 6 shows the different CAD systems for nodule detection in terms of FROC curves, it is evident that our proposed mRFCN system has achieved the most satisfactory performance amongst other tested CAD systems. It should be considered that mRFCN (red line) keeps high sensitivity even in the region where FPs per scan is low. Although MTANNs have a high sensitivity value of over 89% when FPs per scan reaches 4, the sensitivity value of MTANNs drops significantly as FPs per scan becomes small, which is impractical in real-world clinical environment. A summary of our proposed CAD system and other CAD systems comparison in terms of AUROC is depicted in Table VI.

Fig. 7 shows true nodules (marked in green) that were missed in the traditional CNN method, but is detected by our proposed method, when the FPs/scan lies within the range of 1–4 with the sensitivity of 0.9813. The false negatives are marked in red, which have similar appearance to nodules but our proposed system detected them as nonnodules using the characteristics of lung nodules obtained by our mRFCN, such as the

TABLE IV
QUANTITATIVE MEASUREMENTS OF SENSITIVITY, MEAN FROC-SCORE, FP RATE (FPs/SCAN), SPECIFICITY, MEAN ACCURACY, INFERENCE TIME FOR OUR PROPOSED METHOD IN COMPARISON WITH DFCNET IN DIFFERENT MODE (STAND-ALONE OR CLOUD-BASED)

| CAD System | Dataset | System Mode | Sensitivity | mean FROC-score | FPs/scan | Specificity | Mean Accuracy | Inference Time |
|------------------------|------------------|-------------|-------------|-----------------|----------|-------------|---------------|----------------|
| mRFCN (Using mLRPN) | LIDC-IDRI | Stand-Alone | 98.1 | 44.6 | 2.19 | 93.2 | 97.91 | ~180s |
| | | Cloud-Based | 95.2 | 48.3 | 2.1 | 94.5 | 96.7 | ~150s |
| | Clinical Dataset | Stand-Alone | 96.2 | 51.5 | 2.2 | 88.1 | 94.3 | ~175ms |
| | | Cloud-Based | 97.6 | 52.2 | 2.4 | 91.4 | 95.5 | ~120ms |
| mRFCN | LIDC-IDRI | Stand-Alone | 94.4 | 41.6 | 2.21 | 89.2 | 92.1 | ~180s |
| | | Cloud-Based | 95.2 | 42.3 | 2.1 | 90.3 | 90.7 | ~150s |
| | Clinical Dataset | Stand-Alone | 92.2 | 52.7 | 2.9 | 86.1 | 91.3 | ~175ms |
| | | Cloud-Based | 90.3 | 54.1 | 2.4 | 87.4 | 89.5 | ~120ms |
| DFCNet [15] | LIDC-IDRI | Stand-Alone | 89.32 | 29.3 | 2.9 | 83.91 | 86.02 | ~80s |
| | | Cloud-Based | 91.4 | 39.1 | 3.2 | 79.1 | 88.4 | ~90s |
| | Clinical Dataset | Stand-Alone | 96.17 | 53.5 | 1.17 | 83.67 | 86.32 | ~190ms |
| | | Cloud-Based | 93.2 | 55.0 | 1.4 | 80.1 | 88.6 | ~150ms |

TABLE V
QUANTITATIVE RESULTS ASSOCIATED WITH TRAINING AND TESTING ERRORS FOR LIDC-IDRI AND CLINICAL DATASETS

| Dataset | mRFCN | Training Error | Testing Error |
|------------------|-----------------|----------------|---------------|
| LIDC-IDRI [24] | Stand-Alone CAD | 0.00418 | 0.00361 |
| | Cloud-Based CAD | 0.00471 | 0.00298 |
| Clinical Dataset | Stand-Alone CAD | 0.00364 | 0.00288 |
| | Cloud-Based CAD | 0.00394 | 0.00224 |

TABLE VI
AUROC-BASED PERFORMANCE COMPARISON OF EXISTING METHODS VERSUS OUR PROPOSED CAD SYSTEM

| Classifiers | AUROC | Classes |
|-------------|--------|--------------------|
| CNN [12] | 0.7928 | Malignant |
| MTANNs [6] | 0.8355 | Malignant & Benign |
| FCN [13] | 0.8864 | Malignant & Benign |
| MC-CNN [14] | 0.9330 | Malignant & Benign |
| mRFCN | 0.9813 | Malignant & Benign |

example in Fig. 7 third row marked in red. We obtained few false negatives results as the data was not enough to represent that kind of nodules in training phase of our region-based FCN. In Table VI, we can see the area under the FROC curve of the proposed system reaches highest value, i.e., 0.9813, we are confident that our proposed system is the most suitable to use in clinics to detect and diagnose pulmonary nodule since the most CAD system will be applied in clinical environment to detect nodule where the FPs/scan is setting from 1 to 4 mostly. The experimental results presented in Fig. 8 demonstrate the superiority in the generalization of our proposed mRFCN CAD system. To quantitatively evaluate the results for our proposed method, we have measured standard deviation error rate (Std $e_{D,C}$), mean ANODE (mAN) score and processing time (time) of the CT images in the testing set of our clinical dataset with LDA [4], rule-based scheme [26], cascade classifier [27], fuzzy matching [28], Fisher linear discriminant (FLD) [29], SVM [30], feature pyramid network (FPN) [31], sequential forward selection (SFS) [32], cluster-based classifier [33], 3DDCNN [34] techniques. It can be seen in Table VII that our proposed method

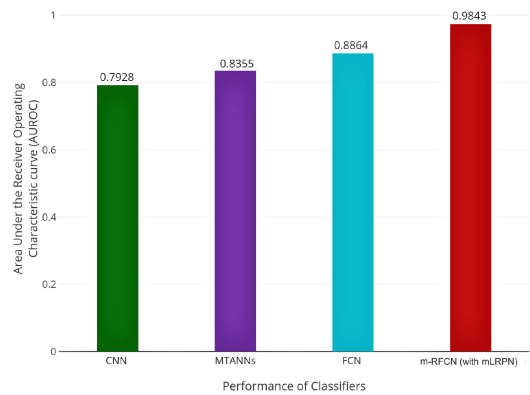


Fig. 8. AUROC-based performance analysis of existing methods versus our proposed CAde system.

achieved comparatively good results for standard deviation error rate, classification sensitivity (sensitivity), FPs per case, and computational duration (of around 219 ± 25.47 s) over other methods.

Qualitative results from the performance comparison between our mRFCN-based CAD system versus state-of-the-art CAD system on having a confidence threshold of 95%. Green represents the ground-truth box. Red boxes are predicted as malignant nodules by our mRFCN method, whereas blue boxes represent benign nodules predictions. Four random cases out of 120 cases from SPH are selected. In Fig. 9, left-most images (a) show the ground truth of lung CT scan, and images (b) on all cases show the predictions of malignant as well as benign nodules prediction of our proposed mRFCN model with confidence scores as high as 92.5%. Table VII describes scoring criteria that are: statistical parameters such as mAN score, standard deviation that is used for both types of error rates, i.e., detection error rate and classification error rate. $Stde_{D,C}$ indicates deviation from perfect detection, the metric $Stde_D$ represents the standard deviation error rate between the radiologists from SPH nodule detection and the detection done by mRFCN and the term $Stde_C$ represents the nodule classification by doctors from SPH and mRFCN classification. Computed results are presented in Table VII.

TABLE VII

COMPARISON OF PROPOSED MRFCN WITH EXISTING METHODS ON CT-SCANS DATASET USING DIFFERENT PERFORMANCE EVALUATION METRICS, NAMELY, SENSITIVITY, STANDARD DEVIATION DETECTION ERROR RATE ($Std_{e_{D,C}}$), FP PER SECTION, FP PER CASE, ANODE SCORE, AND PROCESSING TIME (MINUTES)

| Study | Method | Feature Set | No. of Nodules | Sensitivity | Std $e_{D,C}$ | Fps per Section | Fps per Case | mANODE Score | Time (min) |
|-----------------------------|------------------------|-------------|----------------|-------------|---------------|-----------------|--------------|--------------|------------|
| Armato III et al. 1999 [4] | LDA & Rule Based | 9 | 171 | 70 % | 4.22±0.27 | 3 | 42.2 | 0.543 | - |
| Gurcan et al. 2002 [26] | Rule Based & LDA | 6 | 63 | 84 % | 1.45±0.761 | 5.48 | 1.74 | 0.53 | - |
| Armato III et al. 2002 [27] | Cascade Classifier | 9 | 50 | 80% | 1.24±0.51 | 1.0 | 28 | 0.558 | - |
| Brown et al. 2005 [28] | Fuzzy Matching | 4 | 36 | 86.4 % | 1.55±0.44 | 11 | 1.44 | 0.564 | - |
| Narayanan et al. 2016 [29] | Quadratic, Linear, FLD | 300 | 112 | 62.27% | 1.61±0.99 | 6.89 | 7.05 | 0.5604 | - |
| Narayanan et al. 2018 [30] | SVM | 503 | 1141 | 82.82 % | 1.79±0.64 | 8.11 | 7.80 | 0.71 | - |
| Jaeger et al. 2018 [31] | FPN & Retina U-Net | 64 | 1319 | 73.9 % | 1.79±0.95 | 2.82 | 4.2 | 0.629 | 5-6 |
| Narayanan et al. 2018 [32] | SFS | 39 | 192 | 92.38% | 1.7± 0.6 | 7.75 | 7.37 | 0.597 | - |
| Narayanan et al. 2019 [33] | Cluster-Based & SFS | 300 | 280 | 87.86 % | 1.97±0.90 | 5 | 3.0 | 0.749 | - |
| Masood et al. 2020 [34] | mRPN & 3DDCNN | - | 2361 | 98.4% | 1.4±2.48 | 1.97 | 4.34 | 0.713 | 3.6-4.2 |
| mRFCN | mLRPN & PSSM | - | 892 | 98.1% | 1.4±2.48 | 2.4 | 5.10 | 0.697 | 3.6-4.2 |

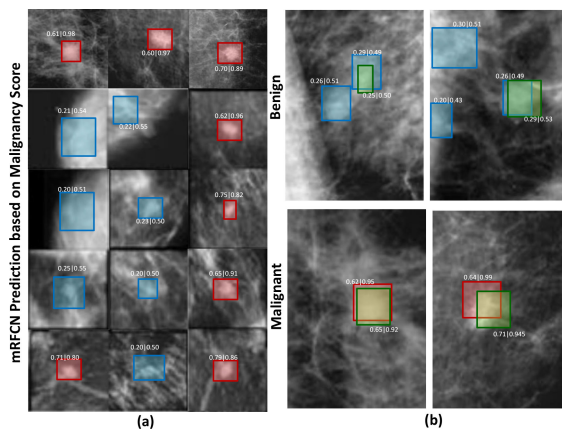


Fig. 9. Malignant (red boxes) and benign nodules (blue boxes) from the mRFCN-based CAde system. Green boxes mark the ground truth and compared to the results produced by our CAde systems are marked by red or blue boxes. Classification is based on the malignancy score at 98.1% sensitivity.

V. CONCLUSION

The solid criteria for a well-performing CAD system are to help the expert radiologist in the process of lung cancer detection as providing them with helpful reference opinion. In this article, we proposed a novel CAD system using mRFCN, where we applied MIP to extract useful information from the nodule dataset combining 3-D view. We proposed mLRPN in our architecture by using deconvolutional layer to improve the original RPN from faster R-CNN. Our CAD system not only indicates the presence of nodule but also gives the location as well as outlines the possible shape of the detected nodule along with the classification of the detected nodule as benign or malignant. Our proposed system was trained and evaluated using LIDC dataset and clinical dataset; the results from our experiments demonstrated that our proposed system has attained the sensitivity of 98.1% and classification accuracy of 97.91%. In the future, we aim to focus on the detection of some micronodules where the diameter is less than 3 mm such that our CAD system works well with all kinds of nodules while maintaining its performance in sensitivity and FP/scan.

REFERENCES

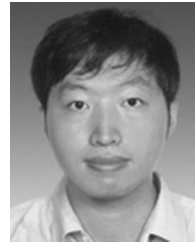
- [1] R. L. Siegel, K. D. Miller, and A. Jemal, "Cancer statistics, 2019," *CA, Cancer J. Clinicians*, vol. 69, no. 1, pp. 7–34, 2019.
- [2] H. Gao, M. Yi, J. Yu, J. Li, and X. Yu, "Character segmentation-based coarse-fine approach for automobile dashboard detection," *IEEE Trans. Ind. Informat.*, vol. 15, no. 10, pp. 5413–5424, Oct. 2019.
- [3] R. K. Samala, H.-P. Chan, C. Richter, L. Hadjiiski, C. Zhou, and J. Wei, "Analysis of deep convolutional features for detection of lung nodules in computed tomography," *Proc. SPIE*, vol. 10950, 2019, Art. no. 109500Q.
- [4] S. G. Armato, III, M. L. Giger, C. J. Moran, J. T. Blackburn, K. Doi, and H. MacMahon, "Computerized detection of pulmonary nodules on CT scans," *RadioGraphics*, vol. 19, no. 5, pp. 1303–1311, 1999.
- [5] K. Suzuki, S. G. Armato, III, F. Li, S. Sone, and K. Doi, "Massive training artificial neural network (MTANN) for reduction of false positives in computerized detection of lung nodules in low-dose computed tomography," *Med. Phys.*, vol. 30, no. 7, pp. 1602–1617, 2003.
- [6] D. Kumar, A. Wong, and D. A. Clausi, "Lung nodule classification using deep features in CT images," in *Proc. Conf. Comput. Robot Vision*, 2015, pp. 133–138.
- [7] X. Ye, X. Lin, J. Dehmshki, G. Slabaugh, and G. Beddoe, "Shape-based computer-aided detection of lung nodules in thoracic CT images," *IEEE Trans. Biomed. Eng.*, vol. 56, no. 7, pp. 1810–1820, Jul. 2009.
- [8] T. Messay, R. C. Hardie, and S. K. Rogers, "A new computationally efficient CAD system for pulmonary nodule detection in CT imagery," *Med. Image Anal.*, vol. 14, no. 3, pp. 390–406, 2010.
- [9] D. Cascio, R. Magro, F. Fauci, M. Iacomi, and G. Raso, "Automatic detection of lung nodules in CT datasets based on stable 3D mass-spring models," *Comput. Biol. Med.*, vol. 42, no. 11, pp. 1098–1109, 2012.
- [10] H. Han, L. Li, F. Han, B. Song, W. Moore, and Z. Liang, "Fast and adaptive detection of pulmonary nodules in thoracic CT images using a hierarchical vector quantization scheme," *IEEE J. Biomed. Health Inform.*, vol. 19, no. 2, pp. 648–659, Mar. 2015.
- [11] A. A. A. Setio *et al.*, "Validation, comparison, and combination of algorithms for automatic detection of pulmonary nodules in computed tomography images: The LUNA16 challenge," *Med. Image Anal.*, vol. 42, pp. 1–13, 2017.
- [12] M. Tan, R. Deklerck, B. Jansen, M. Bister, and J. Cornelis, "A novel computer-aided lung nodule detection system for CT images," *Med. Phys.*, vol. 38, no. 10, pp. 5630–5645, 2011.
- [13] B. van Ginneken, A. A. A. Setio, C. Jacobs, and F. Ciompi, "Off-the-shelf convolutional neural network features for pulmonary nodule detection in computed tomography scans," in *Proc. IEEE Int. Symp. Biomed. Imag.*, 2015, pp. 286–289.
- [14] W. Shen *et al.*, "Multi-crop convolutional neural networks for lung nodule malignancy suspiciousness classification," *Pattern Recognit.*, vol. 61, pp. 663–673, 2017.
- [15] A. Masood *et al.*, "Computer-assisted decision support system in pulmonary cancer detection and stage classification on CT images," *J. Biomed. Inform.*, vol. 79, pp. 117–128, 2018.
- [16] K. Krissian, G. Malandain, N. Ayache, R. Vaillant, and Y. Troussset, "Model based multiscale detection of 3D vessels," in *Proc. Workshop Biomed. Image Anal.*, 1998, pp. 202–210.

- [17] S. Ren, K. He, R. Girshick, and J. Sun, "Faster R-CNN: Towards real-time object detection with region proposal networks," in *Proc. Neural Inf. Process. Syst.*, 2015, pp. 91–99.
- [18] K. Simonyan and A. Zisserman, "Very deep convolutional networks for large-scale image recognition," 2014, *arXiv:1409.1556*.
- [19] J. Long, E. Shelhamer, and T. Darrell, "Fully convolutional networks for semantic segmentation," in *Proc. IEEE Conf. Comput. Vision Pattern Recognit.*, 2015, pp. 3431–3440.
- [20] R. Girshick, "Fast R-CNN," in *Proc. IEEE Int. Conf. Comput. Vision*, 2015, pp. 1440–1448.
- [21] S. Ren, K. He, R. Girshick, and J. Sun, "Faster R-CNN: Towards real-time object detection with region proposal networks," *IEEE Trans. Pattern Anal. Mach. Intell.*, vol. 39, no. 6, pp. 1137–1149, Jun. 2017.
- [22] J. Dai, Y. Li, K. He, and J. Sun, "R-FCN: Object detection via region-based fully convolutional networks," in *Proc. Neural Inf. Process. Syst.*, 2016, pp. 379–387.
- [23] K. He, X. Zhang, S. Ren, and J. Sun, "Deep residual learning for image recognition," in *Proc. IEEE Conf. Comput. Vision Pattern Recognit.*, 2016, pp. 770–778.
- [24] S. G. Armato, III *et al.*, "The lung image database consortium (LIDC) and image database resource initiative (IDRI): A completed reference database of lung nodules on CT scans," *Med. Phys.*, vol. 38, no. 2, pp. 915–931, 2011.
- [25] Y. Tsuchiya, Y. Kodera, R. Tanaka, and S. Sanada, "Quantitative kinetic analysis of lung nodules using the temporal subtraction technique in dynamic chest radiographies performed with a flat panel detector," *J. Digit. Imag.*, vol. 22, no. 2, pp. 126–135, 2009.
- [26] M. N. Gurcan *et al.*, "Lung nodule detection on thoracic computed tomography images: Preliminary evaluation of a computer-aided diagnosis system," *Med. Phys.*, vol. 29, no. 11, pp. 2552–2558, 2002.
- [27] S. G. Armato, III, F. Li, M. L. Giger, H. MacMahon, S. Sone, and K. Doi, "Lung cancer: Performance of automated lung nodule detection applied to cancers missed in a CT screening program," *Radiology*, vol. 225, no. 3, pp. 685–692, 2002.
- [28] M. S. Brown *et al.*, "Computer-aided lung nodule detection in CT: Results of large-scale observer test1," *Acad. Radiol.*, vol. 12, no. 6, pp. 681–686, 2005.
- [29] B. N. Narayanan, R. C. Hardie, and T. M. Kebede, "Analysis of various classification techniques for computer aided detection system of pulmonary nodules in CT," in *Proc. IEEE Nat. Aerosp. Electron. Conf. Ohio Innov. Summit*, 2016, pp. 88–93.
- [30] B. N. Narayanan, R. C. Hardie, and T. M. Kebede, "Performance analysis of feature selection techniques for support vector machine and its application for lung nodule detection," in *Proc. IEEE Nat. Aerosp. Electron. Conf.*, 2018, pp. 262–266.
- [31] P. F. Jaeger *et al.*, "Retina U-Net: Embarrassingly simple exploitation of segmentation supervision for medical object detection," 2018, *arXiv:1811.08661*.
- [32] B. N. Narayanan, R. C. Hardie, and T. M. Kebede, "Performance analysis of a computer-aided detection system for lung nodules in CT at different slice thicknesses," *J. Med. Imag.*, vol. 5, no. 1, 2018, Art. no. 014504.
- [33] B. N. Narayanan, R. C. Hardie, T. M. Kebede, and M. J. Sprague, "Optimized feature selection-based clustering approach for computer-aided detection of lung nodules in different modalities," *Pattern Anal. Appl.*, vol. 22, pp. 559–571, 2019.
- [34] A. Masood *et al.*, "Cloud-based automated clinical decision support system for detection and diagnosis of lung cancer in chest CT," *IEEE J. Transl. Eng. Health Med.*, vol. 8, 2020, Art. no. 4300113.



Anum Masood received the B.Sc. and M.Sc. degrees in computer science from the COMSATS University Islamabad, Islamabad, Pakistan, in 2011 and 2014, respectively. She is currently working toward the Ph.D. degree in computer science with the Department of Computer Science and Engineering, Shanghai Jiao Tong University, Shanghai, China.

She is currently also a Lecturer with the Department of Computer Science, COMSATS University Islamabad. Her research interests include image processing, machine learning, and medical image analysis.



Bin Sheng received the Ph.D. degree in computer science and engineering from The Chinese University of Hong Kong, Hong Kong, in 2011.

He is currently an Associate Professor with the Department of Computer Science and Engineering, Shanghai Jiao Tong University, Shanghai, China. His research interests include image-based rendering, virtual reality, and computer graphics.



Po Yang received the B.Sc. degree in computer science from Wuhan University, Wuhan, China, the M.Sc. degree in computer science from the University of Bristol, Bristol, U.K., and the Ph.D. degree in electronic engineering from Staffordshire University, Stoke-on-Trent, U.K. in 2004, 2006, and 2010, respectively.

He is currently a Senior Lecturer in Large-Scale Data Fusion with the Department of Computer Science, University of Sheffield, Sheffield, U.K. He holds a strong tracking of high-quality

publications and research experiences. He has authored/coauthored more than 40 papers. His research interests include Internet of Things, radio frequency identification (RFID) and indoor localization, pervasive health, image processing, GPU, and parallel computing.



Ping Li (Member, IEEE) received the Ph.D. degree in computer science and engineering from The Chinese University of Hong Kong, Hong Kong, in 2013.

He is currently a Research Assistant Professor with The Hong Kong Polytechnic University, Hong Kong. He has one image/video processing national invention patent, and has excellent research project reported worldwide by ACM TechNews. His research interests include image/video stylization, artistic rendering and synthesis, and creative media.



Huating Li received the Ph.D. degree from Shanghai Jiao Tong University, Shanghai, China, and Pennington Biomedical Research Center, Baton Rouge, LA, USA, in 2011.

She is currently an Associate Professor with the Shanghai Jiao Tong University Affiliated Sixth People's Hospital and the Shanghai Diabetes Institute, Shanghai. Her research interests include the role of cytokines in the development of fatty liver disease, diabetes, and other obesity-related diseases.

Dr. Li was a recipient of the Shanghai Science and Technology Progress Award.



Jinman Kim received the B.S. (Hons.) and Ph.D. degrees in computer science from The University of Sydney, Sydney, NSW, Australia, in 2000 and 2005, respectively.

Since 2006, he has been a Research Associate with Royal Prince Alfred, Camperdown, NSW, Australia. From 2008 to 2012, he was an ARC Postdoctoral Research Fellow, one year leave from 2009 to 2010 to join the MIRALab Research Group, Geneva, Switzerland, as a Marie Curie Senior Research Fellow. Since

2013, he has been with the School of Information Technologies, The University of Sydney, where he was a Senior Lecturer, and became an Associate Professor with School of Computer Science at The University of Sydney, Sydney, Australia, in 2016. His research interests include medical image analysis and visualization, computer-aided diagnosis, and telehealth technologies.



David Dagan Feng (Fellow, IEEE) received the M.Eng. degree in electrical engineering and computer science from Shanghai Jiao Tong University, Shanghai, China, in 1982, and the M.Sc. degree in biocybernetics and Ph.D. degree in computer science from the University of California–Los Angeles (UCLA), Los Angeles, CA, USA, in 1985 and 1988, respectively.

He is currently the Head of the School of Information Technologies, the Director of the Biomedical and Multimedia Information Tech-

nology Research Group, and the Research Director of the Institute of Biomedical Engineering and Technology with The University of Sydney, Sydney, NSW, Australia. He has authored/coauthored more than 700 scholarly research papers, pioneered several new research directions, and made a number of landmark contributions in his field. More importantly, however, is that many of his research results have been translated into solutions to real-life problems and have made tremendous improvements to the quality of life for those concerned.

Dr. Feng is the recipient of the Crump Prize for Excellence in Medical Engineering at the UCLA. He was the Chair of the International Federation of Automatic Control Technical Committee on Biological and Medical Systems, has organized/chaired more than 100 major international conferences/symposia/workshops, and has been invited to give more than 100 keynote presentations in 23 countries and regions. He is a Fellow of the Australian Academy of Technological Sciences and Engineering.